

Microstructure analysis of AZ31 magnesium alloy welds using phase-field models

D. Montiel^{a,*}, L. Liu^b, L. Xiao^b, Y. Zhou^b, N. Provatas^{c,a}

^a Department of Materials Science and Engineering, McMaster University, Hamilton, ON, Canada L8S 4L7

^b Department of Mechanical and Mechatronics Engineering, University of Waterloo, Waterloo, ON, Canada N2L 3G1

^c Department of Physics, McGill University, Montreal, QC, Canada H3A 2T8

Received 30 April 2012; received in revised form 6 July 2012; accepted 8 July 2012

Available online 17 August 2012

Abstract

We use phase-field models to characterize the microstructure present in magnesium AZ31 alloy solidified under welding conditions. We focus our attention on the study of the conditions under which a columnar-to-equiaxed transition (CET) is observed in resistance spot welds. Our simulations show how the size and shape of the columnar and equiaxed regions depend on factors such as cooling rate, temperature gradient and the nature of inoculant particles. Our results are compared with experimental observations. In addition, we contrast our findings with predictions from a previously developed steady-state model for the CET.

© 2012 Acta Materialia Inc. Published by Elsevier Ltd. All rights reserved.

Keywords: Columnar-to-equiaxed transition; Mg alloy; Phase-field simulation; Welding

1. Introduction

It is well known that the microstructure of metals and alloys, which is largely determined by the conditions present during solidification, influences the thermomechanical properties of a given material. An important phenomenon observed in a wide range of solidification processes is the columnar-to-equiaxed transition (CET) [1], a morphological transition that plays an important role in engineering processes such as casting and welding, but whose properties remain poorly understood.

The CET can be defined as a change in dendritic growth regimes occurring during solidification. It is characterized by a morphological transition of the solidifying phase microstructure from columnar domains to equiaxed dendritic grains. Several experimental [2–13], theoretical [14–18] and computational [19–26] studies have been made to understand the nature of the CET, as well as the influence of material parameters and experimental conditions under

which it occurs. This knowledge is important in order to control solidification conditions to obtain a desired microstructure, particularly in the process of welding, where the CET is prevalent.

The first theoretical model for the CET in a binary alloy was developed by Hunt in 1984 [14]. The selection of either columnar or equiaxed growth is assumed to be determined by competition between a columnar solidification front and equiaxed grains formed ahead of the front by nucleation. Hunt's model is applied to steady-state Bridgman growth, in which the solidification front advances at a constant velocity under uniform and constant thermal gradient. Using a simple model to calculate tip velocity [27], a parameter dependent on the thermal gradient, front velocity, solute concentration and nucleation barrier is defined. The value of this parameter represents the volume fraction of the front blocked by equiaxed grains, and determines whether a columnar, equiaxed or mixed microstructure will prevail. Several further efforts to refine Hunt's model have yielded the same qualitative behaviour, albeit with significant quantitative differences [15,16]. Fig. 1 shows an example of a morphological phase diagram obtained

* Corresponding author. Tel.: +1 416 8878313.

E-mail address: montiel@mcmaster.ca (D. Montiel).

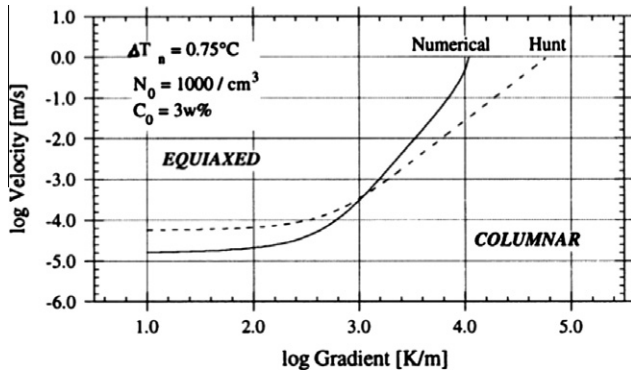


Fig. 1. Columnar-to-equiaxed morphological phase diagram for the Al–Cu system. Comparison between Hunt’s analytical model and the numerical model of Gäumann et al. [16].

numerically by Gäumann et al. for Al–Cu alloys [16]. Their model considers growth at marginal stability [28] and uses Ivantsov’s model [29] to determine the composition profile ahead of the interface. The columnar and equiaxed zones are delineated and compared to the analytical prediction of Hunt’s model. The curves separating different regions shift under different values for solute concentration and nucleation parameters.

1.1. Resistance spot welding: a paradigm for CET

In this work we investigate the CET occurring under conditions typical of those for resistance spot welding (RSW), where the typical cooling rates are much higher than those of conventional casting. RSW is one of the most common welding processes in the automotive industry. In essence, it consists in melting a small volume within a region between two metallic plates by passing a high current through them. Once the current is stopped, solidification of the liquid pool occurs, joining the two plates in the weld region.

In recent years, Mg alloys have received considerable attention in the automotive industry, as considerable weight savings can be achieved by replacing steel or Al alloy parts by Mg alloys. It has been found, however, that the strength of conventional fusion Mg alloy welds is much lower than that of the base material [30,31]. In fusion welds, columnar (or, often, long-branched dendritic arms) and equiaxed grains are often the predominant microstructures [29,32–34]. Experiments and microstructure observations [2,3] confirm that both of these structures are present in resistance spot welds of AZ31 (see Table 1 for composition) and that, apparently, a CET occurs (see Fig. 2). It is well known that, from the mechanical point of view, fine equiaxed grains are preferable to columnar grains. For this

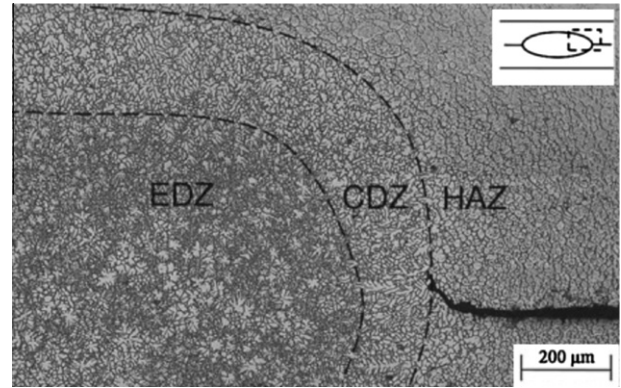


Fig. 2. Heat-affected zone (HAZ), columnar dendritic zone (CDZ) and equiaxed dendritic zone (EDZ) in a resistance spot weld of AZ31 [2].

reason, considerable experimental research has focused on the CET on welds, although only very recently for Mg alloys [2,3,34]. Xiao et al. [3] have investigated the influence of second-phase particles and of added inoculants on the relative size of the columnar and equiaxed regions. The effect of the welding current is also investigated in Ref. [2].

The main purpose of the present work is to investigate the influence of inoculants and thermal conditions on the CET from a theoretical and computational point of view by numerical simulations using phase-field modelling. This analysis is non-trivial due to the fact that solidification occurs under transient, i.e. non-steady-state, thermal conditions typically present on RSW. We thus expect our analysis to provide insight into the applicability of previous steady-state processing conditions, as phase-field models also offer a self-consistent method to model the solidification kinetics of the CET. We will compare our simulation results with steady-state CET predictions from the model by Gäumann et al. (GTK). Our results will confirm that heterogeneous nucleation, as a mechanism for the formation of equiaxed grains, is a sufficient model to fully explain the CET.

The organization of this paper is as follows: Section 2 contains a brief description of the phase-field model for binary alloys used to simulate the dynamics of solidification under non-equilibrium conditions. In Section 3 we describe the algorithm used to incorporate heterogeneous nucleation of grains in the liquid phase, which is coupled with the phase-field model dynamics. Results of our simulations and a comparison to experimental results are presented in Section 6, followed by discussion in Section 7 and conclusions in Section 8.

2. Phase-field model

We use a phase-field model to simulate solidification in the nugget. In this work we use the phase-field model for a dilute binary alloy developed by Echebarria et al. [35] and successfully applied in several alloy solidification studies [36–39]. The details of the derivation of this model can be found in the references provided above. In what follows, we present the equations describing the evolution of the rel-

Table 1
Chemical composition (wt.%) of AZ31 alloy shown in Fig. 2.

Al	Zn	Mn	Si	Ca	RE	Mg
2.92	1.09	0.3	<0.01	<0.01	0.01	Bal.

evant fields as well as a brief description of the implementation of the model. We start by considering a system that consists of solid domains surrounded by an undercooled liquid. A set of continuous fields $[\phi_i]$ is defined. Each of these fields represents the thermodynamic phase present at a particular point in space, having two definite values, 0 and 1, in the bulk liquid and solid phases, respectively. The interface is represented as a region of finite (but non-zero) width W in which the order parameter varies continuously between its two bulk values. Solid grains of different orientations are each represented by a different variable ϕ_i . Solute concentration is represented by an additional field, c . Temperature is represented by the field T . A free energy function f of the local fields is defined and a global free energy F is constructed by integration of f over the volume V of the system:

$$F[c, \vec{\phi}, T] = \int dV \left\{ \sum_{i=1}^N \frac{1}{2} |\epsilon(\vec{\phi}) \nabla \phi_i|^2 + f(c, \vec{\phi}, T) + f_{int}(\vec{\phi}) \right\}, \quad (1)$$

where the first term of the integrand ($\epsilon(\vec{\phi})$ is an anisotropic gradient energy coefficient between a solid and a liquid phase or two solid phases with different orientation) contributes to the interfacial energy. The second term accounts for the bulk free energy density and the third term is the interaction energy between grains of different orientation.

The non-equilibrium dynamics of solidification are described by the integration in time of driving forces for the fields ϕ_i and c [35]:

$$\frac{\partial \phi_i}{\partial t} = -K_\phi \frac{\delta F}{\delta \phi_i} \quad (2)$$

and

$$\frac{\partial c}{\partial t} = \nabla \cdot \left(M(c, \vec{\phi}) \nabla \frac{\delta F}{\delta c} \right), \quad (3)$$

where K_ϕ is a kinetic constant. The coupled equations (2) and (3) are variationally derived from the free energy functional F . In theory these two equations are sufficient to describe the non-equilibrium dynamics of the system. In practice, however, a non-variational term is added in Eq. (3) to correct for a solute-trapping effect arising from the use of an interface width in the model that is much larger than the actual physical value [35,36]. This allows the time step of integration to be significantly larger, dramatically decreasing the computation time.

3. Nucleation

For the CET, a few different mechanisms, such as dendrite fragmentation [9,40,41], grain detachment [8,40], surface nucleation [9,42] and heterogeneous nucleation [40,43] have been proposed to explain the formation of equiaxed grains ahead of the solidification front. However, there does not appear to be conclusive evidence in support of any of these as the predominant mechanism. As several

studies [3,7,8,10,11] have shown that the addition of foreign inoculants promotes the CET, we believe it is a reasonable assumption to consider heterogeneous nucleation as, at least, an important contributing factor for equiaxed grain formation. Thus, our model considers heterogeneous nucleation as the sole mechanism of grain formation.

Unfortunately, given that nucleation is essentially a fluctuation-driven phenomenon that occurs very rarely and in very short time scales, it is difficult to simulate events from noise terms in the phase-field dynamic equations. As an alternative, we follow the stochastic coarse-grained approach of Simmons et al. [44], based on the evaluation of a probability of spontaneous nuclei formation within a certain volume and a certain time interval. The probability that at least one solid nucleus of critical size forms within a homogeneous volume ΔV within a time interval Δt is given by:

$$P = \exp(-J\Delta V\Delta t), \quad (4)$$

where J is the nucleation rate that depends on the local conditions of the liquid. It is given by:

$$J = N\beta^*Z \exp(-\Delta F^*/kT), \quad (5)$$

where N is the nucleation site density, β^* is a frequency factor equal to the reciprocal of the characteristic nucleation time, Z is the Zeldovich factor, k is the Boltzmann constant, T is the absolute temperature and ΔF^* is the nucleation free energy barrier. For a given set of conditions (solute concentration and temperature) for the metastable liquid phase we calculate the value of ΔF^* from classical nucleation theory using bulk and surface energies:

$$\Delta F^* = \frac{16\pi}{3} \frac{h(\theta)\gamma^3}{\Delta f_v^2}, \quad (6)$$

where γ is the solid–liquid interfacial energy, h is a heterogeneous pre-factor that depends on the contact angle θ and Δf_v is the bulk free energy change per unit volume, given by:

$$\Delta f_v = f_S(c_N) - f_L(c_0) - \frac{\partial f_L}{\partial c} \Big|_{c_0} (c_N - c_0) \quad (7)$$

for a binary alloy. In Eq. (7), c_0 is the concentration of the metastable liquid, $c_N = kc_0$ is the concentration of the solid nucleus (k is the partition coefficient in the dilute limit), and $f_S(T, c)$ and $f_L(T, c)$ are the bulk free energy curves for the solid and liquid, respectively. The contact angle θ (and therefore h) depends on the interfacial energy between the liquid and the surface of an inoculant particle. The lower the value of this interfacial energy, the lower the nucleation barrier becomes. Thus, we expect different types of inoculants to yield different values of $h(\theta)$.

While Eqs. (4) and (5) are, in principle, valid only under uniform and constant conditions, we can apply them locally to volume elements and time intervals small enough that conditions do not vary strongly within them.

The details of the implementation of Eqs. (4) and (5) as well as their coupling with the phase-field model are described below in Section 5.

4. Temperature profile

The single most important condition controlling the microstructure during solidification is temperature, and its variation in time (cooling rate) and space (thermal gradient). For this reason it is essential to incorporate a realistic temperature profile, corresponding to actual experimental conditions, into solidification simulations. Temperature in RSW is difficult to measure [34]. For this reason we have opted for the use of a simple thermal conduction model to compute the temperature profile during solidification. We obtain a time-dependent profile by solving the heat equation numerically under known operating conditions of RSW of AZ31. We used approximate experimental values to calibrate our model. A sample 2-D temperature snapshot at the end of the heating stage under welding conditions WP1 (see Section 6) is shown in Fig. 3.

5. Computational procedure

5.1. Phase-Field

We use a computer program developed by Greenwood [45] to simulate the dynamic evolution of solidifying domains within a sample 2-D system [46]. This program performs the numerical integration of Eqs. (2) and (3) on a dynamic adaptive mesh. This mesh, at a given time, comprises square elements of different sizes: smaller ones in regions where sharp variations of the local fields are present (interfaces and grain boundaries), and coarser ones where the fields vary smoothly (bulk phases). As is well known, the advantage in using a non-uniform lattice lies in reducing the number of grid points and, therefore, significantly reducing the number of operations per time step and memory requirements.

5.2. Nucleation

The coupling of nucleation to phase-field dynamics is implemented as follows. First, a certain number of nucle-

ation seeds are placed at random positions within the system of study. This number is determined using the given concentration of inoculant particles N and the total volume of the sample system. The next step is to choose a particular time interval Δt_N as a trial period for the evaluation of the probability of nucleation. Then, at every nucleation trial time, the relevant local conditions of each element (temperature, solute concentration, inoculant concentration) as well as the element area are used to calculate a probability of nucleation within the element using Eq. (4). It should be noted that because the simulation is in two dimensions, a thickness factor d must be introduced in order to compute $\Delta V = d\Delta A$. This factor needs to be such that the average spacing between seeds in the 2-D domain is the same as that of a 3-D domain. This condition gives us $d = N^{-1/3}$. To preserve the validity of Eq. (4), the trial time interval is chosen in such way that nucleation is a relatively rare event ($P \ll 1$). As the phase-field simulation progresses, at every given nucleation trial time, the calculated value of P for each element of the system is compared with a random number (r) between 0 and 1. A nucleation event is then triggered whenever $r < P$. When this happens, a circular grain of size sufficiently larger than the critical radius R^* (obtained from ΔF^*) and random orientation is seeded at the center of the corresponding element. The growth of this grain is subsequently governed by solute diffusion under local non-equilibrium conditions.

6. Results

6.1. Experiments

Five different experimental welding processes for AZ31 (WP1, WP2, WP3, WP4 and WP5), each corresponding to a different set of cooling conditions for solidification, were carried out. Each welding process consist of three stages: (1) the squeezing stage, in which the electrodes press against the plates in order to make a stable contact between the two sheets; (2) the welding stage, in which a high current passes through the plates; and (3) the holding stage

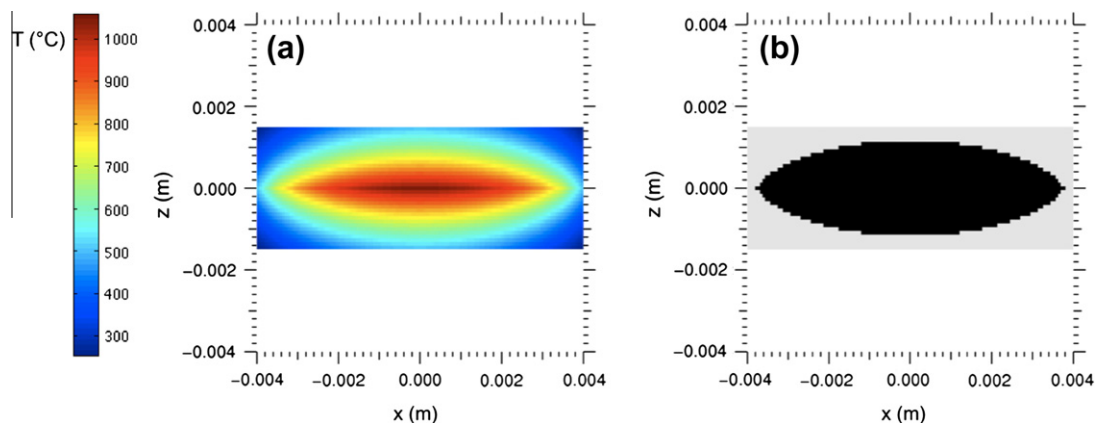


Fig. 3. (a) Temperature profile (model) in the fusion zone at the end of the heating stage under welding conditions WP1 (see Section 6). (b) Fusion zone (dark region) given by the condition $T > T_{\text{melting}}$.

in which the current is either stopped or ramped down to allow cooling by water flowing through the electrodes. For all processes, a force of 4 kN was applied by the electrodes during the squeezing, welding and holding stages. A maximum current of 26 kA was used for the welding stage. The squeezing time was set to 30 cycles (at 60 Hz) and the welding time to 8 cycles. In the holding stage the current was turned off for WP1 and ramped down linearly to 10% of its maximum value for WP3, WP4 and WP5. The duration of the hold stage was set to 0 for WP2 (the electrodes were retracted from the plates), 30 cycles for WP1 and WP3, 40 cycles for WP4 and 50 cycles for WP5. The time-dependent temperature profile for each process (except WP2) was calculated for a volume enclosing the fusion zone (see Section 4). The calculated temperature at the center of the fusion zone is plotted as a function of time in Fig. 4.

For the five welding experimental processes described above, the size of the columnar and equiaxed zones was measured after the samples were cut and polished. Fig. 5 shows a comparison between the size of the columnar regions, measured horizontally from the edge of the fusion zone. In addition to varying the cooling conditions, the effect of adding inoculant particles (Ti, Al_8Mn_5 and Mn) to the weld was studied.

6.2. Simulation

Using the phase-field model coupled with the nucleation algorithms and the calculated thermal conditions for each welding process, we performed a series of simulations of the solidification of the nugget within a region close to the edge of the fusion zone (see Fig. 6). We started by creating base metal solid by allowing a few grains to grow and coalesce under a fixed temperature profile corresponding to that of the onset of the cooling stage. We then let the system

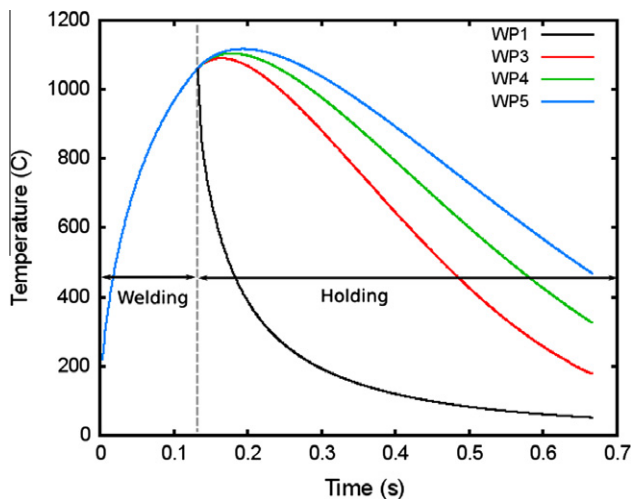


Fig. 4. Calculated temperature at the center of the nugget as a function of time for the cooling conditions of welding processes WP1, WP3, WP4 and WP5.

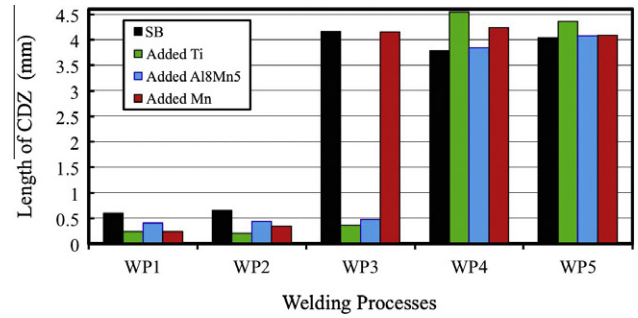


Fig. 5. Size of the columnar region measured horizontally from the edge of the fusion zone for welding processes WP1–WP5 with no added inoculants (SB) and with added Ti, Al_8Mn_5 and Mn particles [47].

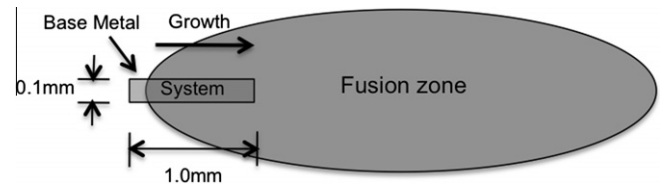


Fig. 6. Fusion zone and simulation domain (rectangular area).

evolve by introducing the calculated thermal profile which promotes domain growth in the direction of the gradient as well as nucleation in locally undercooled regions. We choose a system size of $0.1 \text{ mm} \times 1.0 \text{ mm}$. As an example, Fig. 7 shows simulated solute (Al) concentration maps after complete solidification for thermal conditions WP3 using values of $h(\theta)$ of 3×10^{-4} , 7×10^{-4} and 1.5×10^{-3} . The nucleation site density was set to $N = 1.4 \times 10^{14} \text{ m}^{-3}$. All the remaining relevant parameters used for the simulation are reported in Table 2.

We performed phase-field simulations for the thermal conditions WP1, WP3, WP4 and WP5 using different values for the heterogeneous nucleation prefactor $h(\theta)$. For all the simulations we used $N = 1.4 \times 10^{14} \text{ m}^{-3}$ as well as the parameters shown in Table 2. Fig. 8 summarizes the results of our simulations. The approximate columnar zone size for each welding process is plotted against the prefactor $h(\theta)$. In the same figure, the simulation results are compared with CET predictions from the GTK model (see Section 6.3 below).

6.3. Steady-state CET model

As a reference, we have calculated the steady-state gradient-velocity (G-v) morphological phase diagram for AZ31 using the GTK model for each one of the sets of conditions from our simulations. Fig. 9 shows the CET curves for each value of $h(\theta)$ used. In the plot we also show the G-v trajectories (solidification paths) of the solidus (T_S) and liquidus (T_L) lines corresponding to each of the welding processes WP1, WP3 and WP5. There is a one-to-one correspondence between each solidus (liquidus) point in a trajectory and the time-dependent position of the solidus

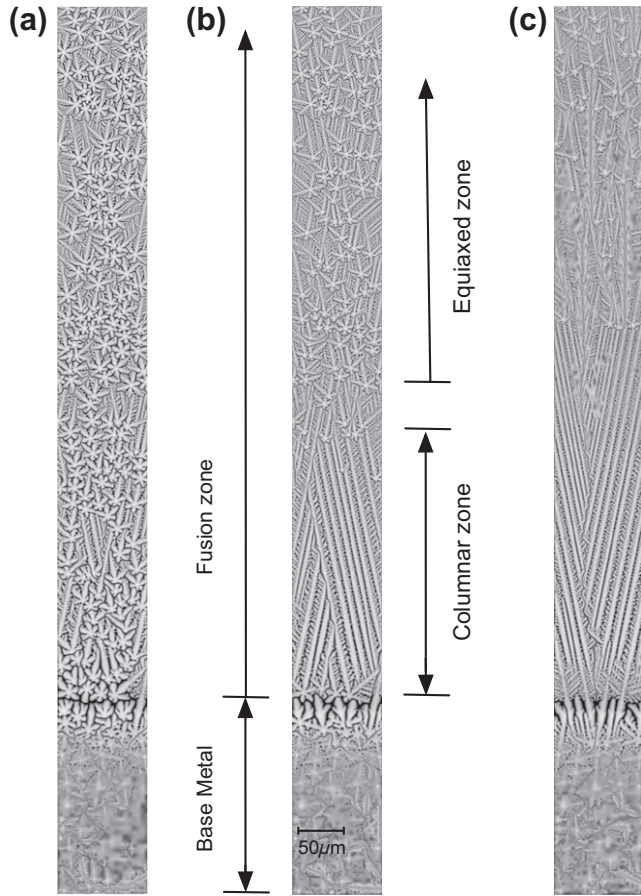


Fig. 7. Solute concentration maps after complete solidification for thermal conditions WP3 and different values of the heterogeneous pre-factor: (a) $h(\theta) = 3 \times 10^{-4}$, (b) $h(\theta) = 7 \times 10^{-4}$ and (c) $h(\theta) = 1.5 \times 10^{-3}$. The nucleation site density was set to $N = 1.4 \times 10^{14} \text{ m}^{-3}$.

Table 2

Physical properties of AZ31, phase-field and nucleation parameters used in the simulations.

Physical properties of model AZ31 alloy	
Chemical composition (wt.%)	Al: 4, Mg: 96
Melting point of Mg ($^{\circ}\text{C}$)	650
Liquidus slope ($^{\circ}\text{C wt.}\%^{-1}$)	-5.5
Partition coefficient	0.4
Solute diffusivity (liquid; $\text{m}^2 \text{ s}^{-1}$)	1.8×10^{-9}
Solute diffusivity (solid; $\text{m}^2 \text{ s}^{-1}$)	10^{-14}
Gibbs–Thomson coefficient (K m)	6.2×10^{-7}
Density (kg m^{-3}) ^a	1740
Solid–liquid interfacial energy (J m^{-2})	0.115
Specific heat ($\text{J kg}^{-1} \text{ K}^{-1}$) ^a	1360
Specific heat of fusion (J kg^{-1}) ^a	3.7×10^5
Thermal conductivity ($\text{W m}^{-1} \text{ K}^{-1}$) ^a	78
Thermal diffusivity ($\text{m}^2 \text{ s}^{-1}$) ^a	3.73×10^{-5}
Phase-field parameters	
Effective interface width, W_0 (m)	10^{-7}
Time step, Δt_ϕ (s)	1.638×10^{-7}
Minimum grid spacing	$0.781 W_0$
Anti-trapping coefficient	0.35355
Nucleation parameters	
Zeldovich factor, Z	0.1
Characteristic frequency, β (s^{-1})	10^{12}
Nucleation trial period Δt_N	$100 \Delta t_\phi$

^a Values for pure Mg.

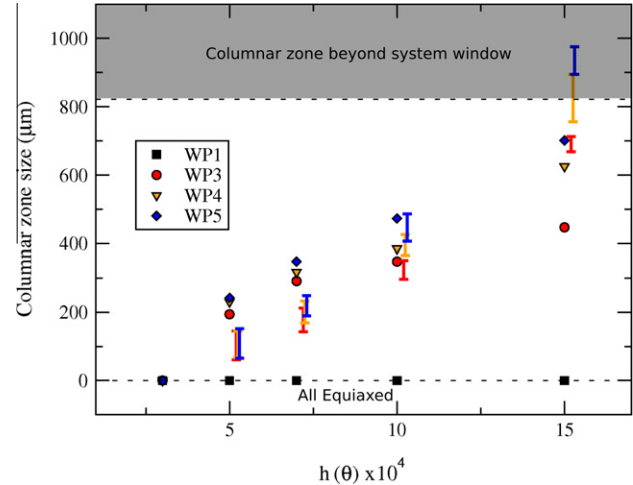


Fig. 8. Approximate columnar zone length vs. $h(\theta)$. (i) Simulation: the dots of different colour (each colour represents a different welding process) mark the approximate measured length of the columnar zone, whenever it is present. (ii) GTK model prediction: the vertical bars of different colours indicate the size range of columnar zones, taken from the intersection points of the CET curves with the G-v trajectories. A value of zero in the ordinate indicates an all-equiaxed growth, while a value above $\sim 820 \mu\text{m}$ (grey zone) indicates an all-columnar growth that extends beyond the system window. (For interpretation of the references to colour in this figure legend, the reader is referred to the web version of this article.)

(liquidus) temperature. Assuming that the front lies somewhere between location of the solidus and liquidus temperatures, the G-v trajectory of the front is assumed to lie somewhere between the corresponding solidus and liquidus trajectories in Fig. 9. The intersection between the trajectories and the CET curves should correspond (approximately) to the region of CET transition if it were the case that transient states obey steady-state behaviour. The columnar size range prediction for each of welding process, taken from the intersection of the CET curves and G-v trajectories, is plotted against the different values of $h(\theta)$ in Fig. 8 (vertical bars).

7. Discussion

Both experimental results and simulations show that the CET depends on both the nature of inoculants and the cooling conditions. In the experimental case the effect of cooling rate dependence is evident when we compare the length of the columnar regions between welding processes WP1–WP2 and WP3–WP5. The much lower cooling rates that characterize the latter cases give rise to significantly larger columnar regions. The same tendency is qualitatively observed in the simulations. Experiments also show a dependence of the CET on the nature of inoculants, although, as Fig. 5 shows, the effect of each type of inoculant on the size of the columnar region appears to be consistent only at high cooling rates (WP1 and WP2).

A direct quantitative comparison between our simulation results and the observed experimental data was not attainable for the following two reasons. (1) For WP1 con-

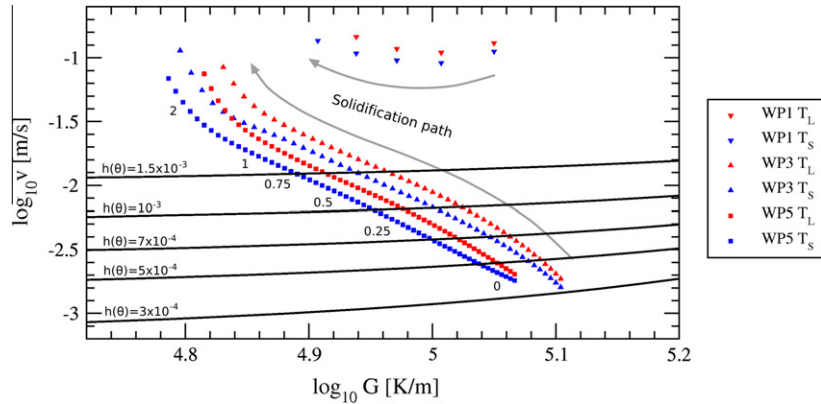


Fig. 9. CET curves (solid lines) for different heterogeneous pre-factors calculated for AZ31 alloy using the GTK model. The solidus (blue) and liquidus (red) dots constitute the G - v trajectories (paths) for the WP1, WP3 and WP5 thermal conditions. WP4 was omitted in order to avoid cluttering. The numbers immediately beside the WP3 and WP5 trajectories correspond to the approximate positions (in mm) of the front throughout the solidification path. (For interpretation of the references to colour in this figure legend, the reader is referred to the web version of this article.)

ditions, where the CET was experimentally observed at an early stage, our simulations predicted equiaxed growth from the onset of solidification, even for very large values of $h(\theta)$ (high nucleation barriers). We believe a reasonable explanation for this is the effect of latent heat diffusion, not accounted for in this work, as an important factor for solidification morphology under the very high cooling rate present in WP1. This hypothesis is supported by the observation of a small but noticeable bump around the melting point in experimental temperature measurements. (2) For WP3–WP5 experiments show a CET occurring in the later stage of solidification, close to the center of the nugget. Our simulation results also show the CET, but because of the limited size of our system we could only observe it within a region close to the fusion zone boundary by decreasing the nucleation barrier to an arbitrarily small value. Increasing the simulation system size to represent a cross-section of the whole solidification domain would have been unfeasible from the computational point of view. A more robust model (one that incorporates latent heat diffusion) along with more computational power would be needed to overcome the issues described above. We believe that future work that addresses these issues could be of significant value.

Regarding the comparison between the phase-field simulations and the CET prediction using the GTK model, which is based on steady-state conditions, there is a clear qualitative agreement. As the plot on Fig. 8 illustrates, both the simulations and the GTK model predict a monotonic increase in the length of the columnar region as the heterogeneous nucleation pre-factor $h(\theta)$ (and nucleation barrier) increases. The same is true for cooling rates. However, among the WP3–WP5 set of conditions, a significantly larger columnar length was observed for lower cooling rates, and both approaches predict all-equiaxed growth for WP1. We believe that the quantitative discrepancies observed can be attributed to the limitation that entails applying the steady-state GTK model to transient

conditions. More specifically, one cannot expect the time-varying solute diffusion field ahead of the front to correspond to a steady-state profile. Given that the phase-field model used in this work has been successfully applied in quantitative predictions before, we are confident that our simulation results can be used as a good benchmark for testing the validity of using the GTK model predictions under transient conditions. It must be noted, however, that the reported length of the columnar zone carries a fair amount of uncertainty in both the simulations and the GTK model predictions. In the simulations, the point in which the CET occurred was measured visually and for most instances it appeared as a gradual transition, making it difficult to define the limits of each zone. For this reason, the simulation values in Fig. 8 were chosen as the positions (with respect to the fusion boundary) where a significant amount of nucleation events was observed. These locations were not readily identifiable in many cases and were not always followed by clear equiaxed growth. For the GTK model, predictions for the columnar length carry an uncertainty due to the inherent difficulty in determining the position of the solidification front within the limits of the solidus and liquidus lines under transient conditions. That is to say, only the positions of the liquidus and solidus temperature lines can be unambiguously determined, while the position of the front, moving within these lines, cannot.

8. Conclusions

The use of a 2-D phase field model for a binary alloy coupled to a probabilistic nucleation mechanism has been shown to be effective in simulating the CET under non-uniform, non-steady-state thermal conditions. We simulated the nugget solidification of AZ31 alloy under conditions typical of RSW. We focused primarily on the effect of cooling rate and the effectiveness of inoculant particles, but our model can be also used to study the effect of other variables, such as inoculant density and average solute concen-

tration. Our results show a reasonable quantitative agreement between simulations and the GTK model for CET.

Acknowledgments

We would like to thank NSERC MagNET for financial support as well as CLUMEQ for providing computational resources. We thank Nana Ofori-Opoku and Michael Greenwood for technical assistance and helpful discussions.

References

- [1] Kurz W, Bezençon C, Gäumann M. *Sci Technol Adv Mater* 2001;2:185.
- [2] Liu L, Xiao L, Feng J, Tian Y, Zhou S, Zhou Y. *Metall Mater Trans A* 2010;41:2642.
- [3] Xiao L, Liu L, Zhou Y, Esmaili S. *Metall Mater Trans A* 2010;41:1511.
- [4] Witzke S, Riquet JP. *Acta Metall* 1982;30:1717.
- [5] Sturz L, Zimmermann G. *Mater Sci Forum* 2006;508:419.
- [6] Canté MV, Cruz KS, Spinelli JE, Cheung N, Garcia A. *Mater Lett* 2007;61:2135.
- [7] Ganaha T, Pearce BP, Kerr HW. *Metall Trans A* 1980;11A:1351.
- [8] Pearce BP, Kerr HW. *Metall Trans B* 1981;12B:479.
- [9] Villafuerte JC, Pardo E, Kerr HW. *Metall Trans A* 1990;21A:2009.
- [10] Kou S, Le Y. *Weld J* 1986;65:305s.
- [11] Kou S, Le Y. *Metall Trans A* 1988;19A:1075.
- [12] Siqueira C, Cheung N, Garcia A. *Metall Mater Trans A* 2002;33A:2107.
- [13] Zimmermann G, Sturz L, Schmitz B, Meyer I. In: *Proc 19th ESA symposium on European rocket and balloon programmes and related research*, ESA SP-671, Bad Reichenhall, Germany; 2009.
- [14] Hunt J. *Mater Sci Eng* 1984;65:75.
- [15] Cockcroft SL, Rappaz M, Mitchell A, Fernihough J, Schmalz AJ. *Materials for advanced power engineering*, vol. II. Dordrecht: Kluwer; 1994. p. 1145.
- [16] Gäumann M, Trivedi R, Kurz W. *Mater Sci Eng* 1997;A226–228:763.
- [17] Flood SC, Hunt JD. *J Cryst Growth* 1987;82:543.
- [18] Flood SC, Hunt JD. *J Cryst Growth* 1987;82:552.
- [19] Kumar A, Dutta P. *J Mater Sci* 2009;44:3952.
- [20] Li J, Wang J, Yang G. *J Cryst Growth* 2007;309:65.
- [21] Mirihanage WU, McFadden S, Browne DJ. *Mater Sci Forum* 2010;649:355.
- [22] Wang CY, Beckermann C. *Metall Mater Trans A* 1994;25A:1081.
- [23] Viardin A, Sturz L, Zimmermann G, Apel M. *J Phys Conf Ser* 2011;327:012004.
- [24] Badillo A, Beckermann C. *Acta Mater* 2006;54:2015.
- [25] Dong HB, Lee PD. *Acta Mater* 2005;53:659.
- [26] Noepfel A, Budenkova O, Zimmermann G, Sturz L, Mangelinck-Noël N, Jung H, et al. *Int J Cast Metal Res* 2009;22:34.
- [27] Hunt JD. In: *Proc conf on solidification and casting of metals*, Sheffield, July 1977. London: Metals Society; 1979. p. 1.
- [28] Langer JS, Müller-Krumbhaar H. *J Cryst Growth* 1977;42:11.
- [29] Kurz W, Fisher D. *Fundamentals of solidification*. Aedermannsdorf, Switzerland: Trans Tech SA; 1989.
- [30] Wu SH, Huang JC, Wang YN. *Metall Mater Trans A* 2004;35A:2455.
- [31] Liu LM, Zhang ZD, Song G, Wang L. *Metall Mater Trans A* 2007;38A:649.
- [32] McCartney D. *Int Mater Rev* 1989;34:247.
- [33] David SA, Vitek JM. *Int Mater Rev* 1989;34:213.
- [34] Wang YR, Feng JC, Zhang ZD. *Sci Technol Weld Joi* 2006;11:555.
- [35] Echebarria B, Folch R, Karma A, Plapp M. *Phys Rev E* 2004;70:061604.
- [36] Ofori-Opoku N, Provatas N. *Acta Mater* 2010;58:2155.
- [37] Amooezaei M, Gurevich S, Provatas N. *Acta Mater* 2010;58:6115.
- [38] Amooezaei M, Gurevich S, Provatas N. *Acta Mater* 2012;60:657.
- [39] Gurevich S, Karma A, Plapp M, Trivedi R. *Phys Rev E* 2010;81:011603.
- [40] Kou S. *Welding metallurgy*. Hoboken (NJ): John Wiley & Sons; 2003.
- [41] Matsuda F, Nakagawa H, Nakata K, Ayani R. *Trans JWR I* 1978;7:111.
- [42] Ganaha T, Kerr HW. *Met Technol* 1978;5:62.
- [43] Qiu D, Zhang MX, Taylor JA, Fu HM, Kelly PM. *Acta Mater* 2007;55:1863.
- [44] Simmons J, Shen C, Wang Y. *Scripta Mater* 2000;43:935.
- [45] Greenwood M. *Using phase-field modeling with adaptive mesh refinement to study elasto-plastic effects in phase transformations*, PhD thesis, McMaster University; 2008.
- [46] Provatas N, Goldenfeld N, Dantzig J. *J Comput Phys* 1999;148:265.
- [47] Xiao L. *Microstructure refinement and mechanical property improvement of AZ31 magnesium alloy resistance spot welds due to inoculants*, PhD thesis, University of Waterloo; 2012.